Article

AMERICAN SCIENTIFIC PUBLISHERS

Journal of Nanoscience and Nanotechnology
Vol. 20, 1–6, 2020
www.aspbs.com/jnn

Effect of Nickel Doping on the Properties of Hydroxyapatite Nanoparticles

P. Kurinjinathan[1], K. Thanigai Arul[1,*], J. Ramana Ramya[2], E. Manikandan[1,3,4,*], H. H. Hegazy[5,6], Ahmad Umar[7,*], H. Algarni[5], and Naushad Ahmad[8]

[1] *Energy and Biophotonics Lab, Department of Physics, AMET Deemed to be University, Kanathur, Chennai 603112, Tamil Nadu (TN), India*
[2] *Crystal Growth Centre, Anna University, Chennai 600025, Tamil Nadu, India*
[3] *Department of Physics, TUCAS Campus, Thiruvalluvar University, Thennangur 604408, Tamil Nadu, India*
[4] *UNESCO-UNISA AFNET in Nanosciences/Nanotechnology, College of Graduate Studies, University of South Africa, Muckleneuk Ridge, P.O. Box 392, Pretoria-South Africa*
[5] *Department of Physics, Faculty of Science, King Khalid University, P.O. Box 9004, Abha, Saudi Arabia*
[6] *Department of Physics, Faculty of Science, Al-Azhar University, 71524 Assiut, Egypt*
[7] *Depertment of Chemistry, Faculty of Arts and Sciences and Promising Center for Sensors and Electronic Devices (PCSED), Najran University, Najran-11001, Saudi Arabia*
[8] *Department of Chemistry, College of Science, King Saud University, Riyadh-11451, Kingdom of Saudi Arabia*

Herein, we studied the effect of nickel (Ni) doping on the properties of hydroxyapatite (HAp) nanoparticles synthesized by facile ultrasonication assisted wet chemical synthesis process. Various doping concentrations of nickel, i.e., 0.01 M, 0.05 M and 0.10 M, were used to dope into hydroxyapatite nanoparticles. The synthesized nanoparticles were characterized by X-ray diffraction (XRD) pattern, scanning electron spectroscopy (SEM), Fourier transform infrared (FTIR) spectroscopy, UV-Visible spectroscopy and Raman-scattering spectroscopy. The detailed structural characterizations confirmed that the crystallite sizes of the Ni-doped hydroxyapatite nanoparticles were reduced up to 53% compared to pure hydroxyapatite upon the doping of different concentrations of Ni ions. The agglomeration in the nanoparticles was also reduced by increasing the doping concentration of Ni ions. The XRD studies revealed that the average crystallite size of the synthesized Ni-doped HAp was decreased with increasing the concentration of Ni^{2+} ion doping and this observation was well-consistent with the SEM results. The FTIR and Raman studies well-confirmed the formation of pure HAp and Ni-doped HAp. Further, doping with Ni creates a new level of energy between the conductive band and the valence band and hence with increasing the concentration of Ni^{2+}, the intensity in the UV-vis spectra was enhanced.

Keywords: Hydroxyapatite, Ni^{2+} Doping, Nanoparticles.

1. INTRODUCTION

As one of the most important synthetic biomaterials mainly composed of Ca, P and O, the hydroxyapatite (HAp, $Ca_{10}(PO_4)_6(OH)_2$) possess almost similar compositions of mammalian hard tissues, thus used for several important bone and teeth related applications, to name a few, bone grafting, dental filling, implantation, and other bone related applications [1–3]. As an important bioactive and biocompatible biomaterials, the HAp has abilities to bond with hard tissues without any connective tissues [2]. As for as the mineral components of the mammalian bones are concerned, these are not only mainly made of Ca, P and O in non-stoichiometric manner but also possess trace amount of various ions such as Sr^{2+}, $SiO4^{4-}$, Mg^{2+}, Ni^{+}, F^{-}, Na^{+}, $SO4^{2-}$ and so on as trace amount of such ions play an important role to develop hard tissues [3, 4]. Interestingly, the synthetic HAp does not possess these traces of ions resulting inferior ability to accelerate the bone reformation process compared to the natural bone tissues [5]. Therefore, to enhance various properties of synthetic HAp, it is important to dope it with some specific ions such as Sr^{2+}, $SiO4^{4-}$, Mg^{2+}, Ni^{+}, F^{-}, Na^{+}, $SO4^{2-}$ [5–7]. The crystal structure of HAp

---

*Authors to whom correspondence should be addressed.

1533-4880/2020/20/001/006 doi:10.1166/jnn.2020.17182

is composed of Ca^{2+}, OH^- and $(PO_4)^{3-}$ and it possesses an excellent ion exchange capacity, thus the Ca^{2+} ions in the crystal lattice can be replaced by various ions such as Ag^+, Co^{2+}, Fe^{3+}, Mg^{2+}, etc. [5–7]. The substitution of magnetic metal ions such as Fe^{3+}, Co^{2+} in HAp nanoparticles was prepared and used in MRI (Magnetic Resonance Imaging), cell separation, targeted drug delivery and hyperthermia [8, 9]. Ammar et al. have synthesized Mg and Ni doped silicate hydroxyapatite and examined their *in vitro* bioactivities and confirmed that the Ni^{2+}-doped silicate hydroxyapatite possess good antibacterial properties against *E. coli* and *P. aeruginosa* [10]. Aguila et al. demonstrated synthesis and structural properties of transition metal ions doped calcium hydroxyapatite by microwave assisted sol–gel process at 150° [11]. Salehi et al. reported the effects of metal ions (Co, Ni) doping concentration in hydroxyapatite and their photocatalytic activities towards dye-degradation [12]. Kamieniak et al. examined the catalytic activities of methance oxidation on palladium and Ni doped hydroxyapatite based on metal and metal oxide redox cycles [13]. Using nickel-doped biphasic calcium phosphate/graphene nanoplatelets composites, Baradaran et al. demonstrated some biomedical applications in which biological behaviour of osteoblast cell culture was investigated for several days [14].

In this paper, we report the effect of Ni-doping (0.01 M, 0.05 M and 0.10 M) on the properties of hydroxyapatite (HAp) nanoparticles synthesized by facile ultrasonication assisted wet chemical synthesis process. The synthesized nanoparticles were examined by several techniques to understand the effect of Ni-doping on the structural, morphological, compositional and optical properties.

2. EXPERIMENTAL DETAILS

2.1. Materials

Calcium nitrate tetrahydrate ($Ca(NO_3)_2 \cdot 4H_2O$) and diammonium hydrogen phosphate $(NH_4)_2HPO_4$ and 25% of ammonia solution were bought from Merck. Nickel (II) nitrate hexahydrate ($Ni(NO_3)_2 \cdot 6H_2O$) was bought from Sigma-Aldrich. All the chemicals were used as received without further purifications.

2.2. Synthesis of Hydroxyapatite (HAp) Nanoparticles

For the synthesis of hydroxyapatite nanoparticles, 1 M calcium nitrate tetrahydrate ($Ca(NO_3)_2 \cdot 4H_2O$) and 0.6 M diammonium hydrogen phosphate ($(NH_4)_2HPO_4$) were dissolved in the double distilled water. Consequently, the prepared Calcium nitrate tetrahydrate solution was drop-wise added to the diammonium hydrogen phosphate solution under magnetic stirring and ultrasonication assisted route. Further, to maintain the pH = 10, several drops of ammonia solution was added in the resultant solution and ultrasonicated under stirring for 30 min. After completion of the reaction, the obtained precipitate was centrifuged. Finally, the obtained material was washed with deionized (DI) water and ethanol, sequentially and finally dried in a vacuum oven at 80 °C. The dried samples were mechanically grinded and denoted as pristine.

2.3. Synthesis of Ni-Doped Hydroxyapatite Nanoparticles

For the synthesis of nickel doped HAp ($Ni_XCa_{10-X}(PO_4)_6OH_6$), desired concentration of Ni ($X = 0.01$ M, 0.05 M, 0.1 M) from the nickel (II) hexahydrate was added along with 1 M calcium nitrate tetrahydrate, both dissolved in double distilled water and stirred for 30 min. Consequently, the prepared nickel–calcium nitrate solution was drop-wise added to 0.6 M of diammonium hydrogen phosphate. Further, to maintain the pH = 10 of the solution, few drops of ammonia solution was added and obtained solution was ultrasonicated under stirring for 30 min. After completion of the reaction, the obtained precipitate was centrifuged and washed with DI water and ethanol and finally dried in a vacuum oven at 80 °C. The prepared powders were grinded and denoted as 0.01 Ni-HAp (0.01 M Ni doped), 0.05 Ni-HAp (0.05 M Ni doped) and 0.1 Ni-HAp (0.1 M Ni doped).

2.4. Characterizations of the Synthesized HAp and Ni-HAp Nanoparticles

The phase identification of the samples was performed by X-ray Powder Diffraction (XRD) using analytical diffractometer (PANalytical) with $CuK\alpha = 1.5406$ Å radiation in the 2θ range of 10° to 70° with a step size of 0.040. The morphologies of the prepared materials were analyzed by Scanning Electron Microscopy (SEM). The functional groups of the samples were collected in the mid-IR region of 4000 cm^{-1}–400 cm^{-1} using FTIR spectrometer (JASCO FT/IR6300). Raman studies were also performed using a 1064 nm laser wavelength. The optical properties of the samples were studied by UV-Vis spectrophotometer in the region of 200–800 nm using Jasco 750 series in Diffuse Reflectance Spectroscopy (DRS) mode.

3. RESULTS AND DISCUSSION

3.1. Structural, Morphological and Compositional Properties of Pure and Ni-Doped HAp Nanoparticles

3.1.1. X-ray Diffraction Analysis

The crystal properties and characteristics of the synthesized HAp and Ni-doped HAp nanoparticles were examined by X-ray diffraction (XRD) and observed results are shown in Figure 1. The peaks appeared in the XRD pattern of HAp indicate the formation of the crystalline phases. The XRD pattern revealed several peaks which belong to the HAp crystallites and correspond to the reported literature and JCPDS card no. 09-0432 [15–17]. Except HAp peaks, no peak related with other impurities were seen in

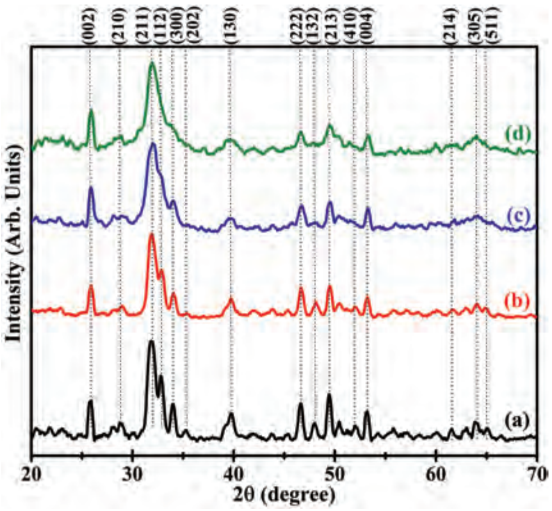

Figure 1. Typical XRD patterns of (a) pure HAp, (b) 0.01 M Ni-doped HAp, (c) 0.05 M Ni-doped HAp, and (d) 0.1 M Ni-doped HAp nanoparticles.

the pattern which revealed that the prepared material is pure HAp without any significant impurity. Interestingly, the diffraction peaks of HAp exhibited distinct and narrower peaks suggesting the enhanced crystallinity of the synthesized HAp. It was observed that with the addition of nickel ions in HAp reduces the diffraction peak intensities which were confirmed from the widening of the full width at half maximum (FWHM) of major planes. With the increase in the nickel ion concentrations, some of the planes like (112) and (300) were diminished [22, 23]. Nickel ion incorporation decreased the crystallite size of Ni-HAp (55.3%) compared to pure HAp. The crystallite size of the samples was calculated by Scherrer equation as mentioned below:

$$\tau = K\lambda/\beta\mathrm{Cos}\theta$$

Where K is a constant, λ is the wavelength of monochromatic radiation, β is defined as diffraction peak for full width half maximum. According to the Scherrer equation, the average crystallite size of the synthesized Ni-doped HAp was decreased with increasing the concentration of Ni^{2+} ion doping. Table I exhibits the typical crystallite sizes of the synthesized Ni-HAp nanoparticles based on various concentration of Ni^{2+} ions doping. The reduced crystallite size of the synthesized Ni-doped HAp could be attributed to the replacement of calcium by the Ni ions in the apatite structure [17]. Further analysis showed a decrease in crystallinity with an increase in the doping percentage. No such peak broadening has been observed in the present study, which implies that Ni^{+2} doping has not greatly distorted the apatite crystal. However, the observed variation in the crystal parameter was likely due to the smaller Ni^{+2} ionic radius (0.72 Å) compared to Ca^{+2} (0.99 Å).

Table I. Crystallite size of pure and Ni-doped HAp nanoparticles.

Samples	Average crystallite size (nm) (±0.01)
Pure HAp	29.09
0.01Ni-doped HAp	16.57
0.05Ni–Ni-doped HAp	14.33
0.1Ni–Ni-doped HAp	13.66

3.1.2. Scanning Electron Microscopy Studies

The morphologies of the synthesized pure and Ni-doped HAp materials were examined by scanning electron microscopy (SEM). Figure 2 exhibits the typical SEM images of pure and Ni-doped HAp materials which clearly revealed that the synthesized materials possess nanoscale dimension particles, hence termed them as 'nanoparticles.' It is clearly seen from the SEM images of the pure HAp that the synthesized material possess agglomerated non-uniform spheres composed of nanodimensions particles (Figs. 2(a and b)). The typical sizes of the non-uniform spheres are in the range of 400 ± 50 nm. Interestingly, the

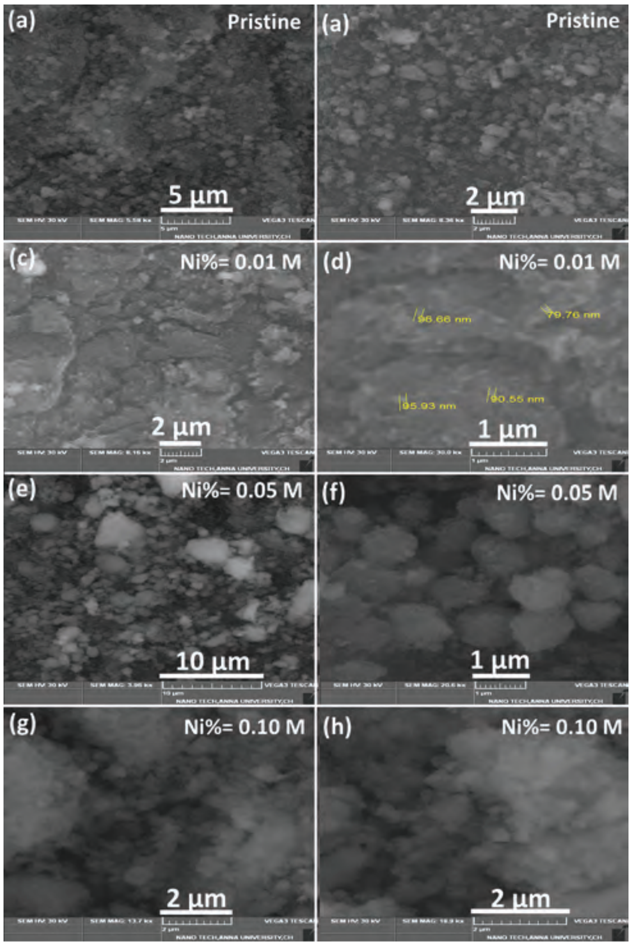

Figure 2. Typical SEM images of (a, b) pristine, (c, d) 0.01 M Ni-doped HAp, (e, f) 0.05 M Ni-doped HAp and (g, h) 0.1 M Ni-doped HAp nanoparticles.

average particle sizes were reduced with increasing the doping concentration of nickel ions in HAp (Figs. 2(c–f)). In addition, the doping of different concentration of nickel ions also influence the morphologies of the synthesized particles, however, all the samples preserved spherical shaped morphologies of the synthesized Ni-doped HAp particles. As observed from the SEM images, the sample morphologies were slightly influenced by the increase in the Ni^{2+} concentration.

3.1.3. Fourier Transform Infrared Spectroscopy Analysis

The chemical compositions and functional groups of the synthesized pure and Ni-doped HAp nanoparticles were examined by Fourier transform infrared (FTIR).

Figure 3 exhibits the typical FTIR spectra of pure and Ni-doped HAp nanoparticles which show the origination of various well-defined peaks of different functional groups. As observed, various well-defined peaks are seen in the FTIR spectra. The FTIR peaks appeared at 469 cm^{-1} was due to vibrational mode of P–O, 567 cm^{-1} was because of the P–O asymmetric stretching mode while the presence of well-defined peak at 603 cm^{-1} was due to O–P–O bending mode [18]. The first indication for HAp formation is a strong complex wide FTIR band centered around 1000–1100 cm^{-1} due to symmetric stretching vibration mode for PO_4 group [19]. Adsorbed water provided two band types, O–H bending (1642 cm^{-1}) and O–H stretching (3400–3600 cm^{-1}), due to the presence of hydroxy group in the apatite. In Ni-HAP, the peak at 1642 cm^{-1} became wider, and this could be due to crystal deformation [20]. The crystalline powder generates around 3577 cm^{-1} and 3427 cm^{-1} two characteristic stretching modes of O–H bands. This may be because of the mild variation in that ionic environment in the crystal lattice which leads to alteration in the stretching field. All the samples show a common peak of H bonded OH stretching at 3457 cm^{-1}. A new peak appeared at 3427 cm^{-1} that could be attributed to the stretching of free OH, which becomes more intense with increasing the doping of Ni^{2+} ions [21]. The characteristic of stretching and vibration modes of the hydroxyl group was found at 3577 cm^{-1} and 1642 cm^{-1}, respectively. The broadband was noticed at 3577 cm^{-1} due to the presence of water molecule [22]. Due to the CO_2 adsorption from the atmosphere, bands at 1385 cm^{-1} and 872 cm^{-1} corresponding to $(CO_3)_{2-}$were seen [23].

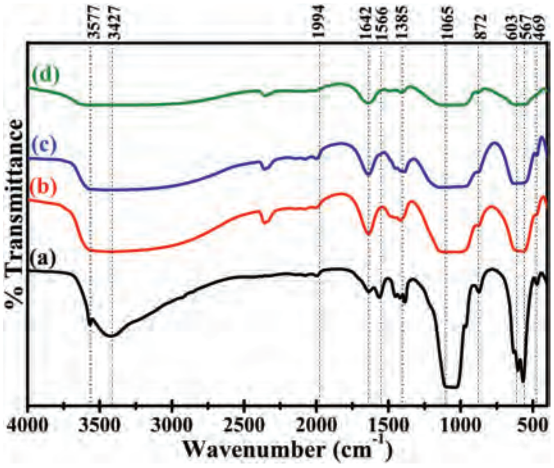

Figure 3. FTIR spectra of (a) pure HAp, (b) 0.01 M Ni-doped HAp, (c) 0.05 M Ni-doped HAp, and (d) 0.1 M Ni-doped Hap nanoparticles.

3.1.4. Raman-Scattering Analysis

To examine the scattering properties, the synthesized pure and Ni-doped HAp nanoparticles were examined by Raman-scattering measured at room-temperature. Figure 4 exhibits the typical Raman-scattering spectra of the synthesized pure and Ni-doped HAp nanoparticles. The Raman-scattering spectra of all samples exhibited a sharp, dominated and strong band at 963 cm^{-1} which was associated with the symmetric (ν_1) P–O–P stretching mode of the free tetrahedral phosphate ion and characteristic band of HAp [24]. The peak appeared at 963 cm^{-1} is the characteristic Raman peak for pure HAp and appeared in all pure and Ni-doped HAp nanoparticles [24]. Interestingly, the peak intensities of the phosphate ν_1 stretching mode band appeared at 963 cm^{-1} was decreased with increasing the concentration of Ni-ion doping into HAp which could be due to the replacement of Ca ions with Ni ions into the lattices of HAp, resulting decrease in the P–O bonding strength [25]. The short peaks appeared at 1045 cm^{-1} in all samples are due to ν_3 vibration mode of PO_4^{3-} group [26, 27]. In addition to this, two small peaks are also seen at 593 cm^{-1} referred as $\nu_4(PO_4)$ mode and 433 cm^{-1} assigned as $\nu_2(PO_4)$ mode. The synthesized pure HAp exhibits several other small peaks at 489 cm^{-1}

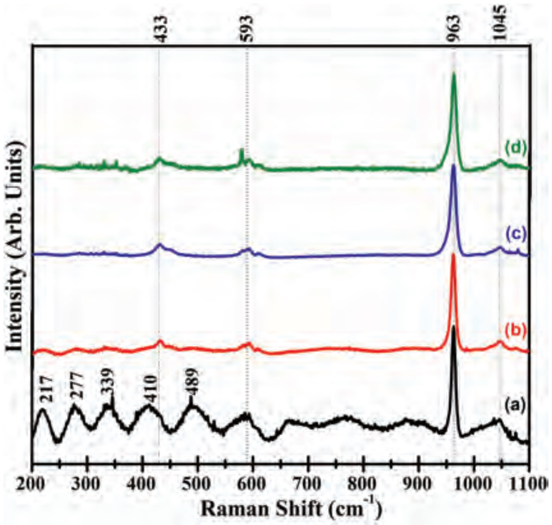

Figure 4. Raman spectra of (a) pure HAp, (b) 0.01 M Ni-doped HAp, (c) 0.05 M Ni-doped HAp, and (d) 0.1 M Ni-doped Hap nanoparticles.

(ν_2(PO$_4$) mode), 410 cm^{-1} (ν_2(PO$_4$) mode), 339 cm^{-1} (Ca(II)–OH ν_3 stretching mode), 277 cm^{-1} (Ca-PO$_4$ mode) and 217 cm^{-1} (Ca-PO$_4$ mode) [24, 25]. Interestingly, these small peaks are vanishing after doping the HAp with Ni ions. The observed Raman-scattering results are consistents with the FTIR studies.

3.2. Optical Properties of Pure and Ni-Doped HAp Nanoparticles

The optical properties of the synthesized pure and Ni-doped HAp nanoparticles were examined by UV-Visible spectroscopy at room-temperature. Figure 5 depicts the typical UV-vis. spectra of pure and Ni-doped HAp nanoparticles. The synthesized pure HAp exhibited a defined UV absorption peak at 301 nm for which the intensity was further reduced in case of nickel doped HAp nanoparticles [28, 29]. All the Ni-doped HAp nanoparticles exhibited a broad peak at 560 nm. The intensity of this peak was not only increases with increasing the concentration of Ni-ions in the HAp crystallites but also the peaks were slightly red-shifted. The high intensities and red-shifts in the absorption bands with Ni^{2+} doping was due to the possible acceleration of the sp–d orbital exchange interaction between the band and localized d-electrons of Ni^{2+} ions [10]. Such phenomena, i.e., high the intensity and red-shift peaks with increasing the concentration of Ni^{2+} ions clearly revealed the successful incorporation of Ni^{2+} ions in place of Ca^{2+} [10]. Doping with Ni creates a new level of energy between the conductive band and the valence band. The valence band electrons absorb higher wavelength photons and create new impurity level, first by transferring to impurity level and then by absorbing other photons transferred to the conduction band. Therefore, significantly, the UV-visible absorption of Ni-HAp is drastically enhanced compared to pure HAp. This remarkable absorption of Ni-HAp is attributed to Ni in various coordinating environments caused by the HAp crystal substitution of Ni by Ca. These doped Ni^{2+} ions, meanwhile, can introduce an energy level into the electronic band structures of Ni-doped HAp.

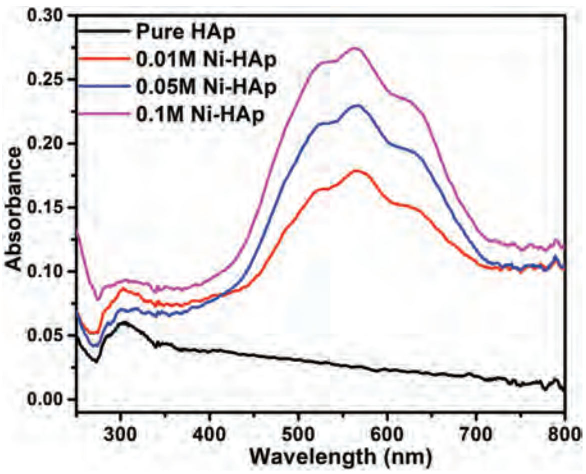

Figure 5. UV-visible spectra of (a) pristine, (b) 0.01 M Ni-HAp, (c) 0.05 M Ni-HAp and (d) 0.1 M Ni-HAp nanoparticles.

4. CONCLUSIONS

In summary, pure and Ni-doped HAp nanoparticles were synthesized by facile ultrasonication assisted wet-chemical route and systematically characterized by several techniques. The XRD results revealed that with increasing the concentration of Ni^{2+} ions into HAp, the crystallites sizes were reduced. Thus, the observed crystallite sizes for pure HAp, 0.01 M, 0.05 M and 0.1 M Ni-doped HAp were 29.09 nm, 16.57 nm, 14.33 nm and 13.66 nm, respectively. Further, FTIR and Raman analysis were also confirmed the appreciable variation in the hydroxyl and phosphate groups. UV visible spectra revealed the energy transfer, ion exchange phenomena of the calcium apatite and showed enhanced absorbance at higher concentration. Due to good structural, compositional and optical properties, the synthesized nanoparticles can efficiently be used in various biomedical applications such as drug delivery, antibacterial and antifungal properties and so on.

Acknowledgments: The authors gratefully thank the Deanship of Scientific Research at King Khalid University for the financial support through research groups program under grant number (R.G.P.2/18/40).

References and Notes

1. Ahamed, S.I., Beevi, A.H., Begum, K.M., Nivetha, S. and Ayeshamariam, A., **2017**. Cytotoxic effect of green synthesized Co/HAp nanocomposites against MCF-7 cell line. *Journal of Bionanoscience*, *11*(5), pp.384–390.
2. Canillas, M., Rivero, R., García-Carrodeguas, R., Barba, F. and Rodríguez, M.A., **2017**. Processing of hydroxyapatite obtained by combustion synthesis. *Boletín de la Sociedad Española de Cerámica y Vidrio*, *56*(5), pp.237–242.
3. Levy, M., Quarta, A., Espinosa, A., Figuerola, A., Wilhelm, C., García-Hernández, M., Genovese, A., Falqui, A., Alloyeau, D., Buonsanti, R. and Cozzoli, P.D., **2011**. Correlating magneto-structural properties to hyperthermia performance of highly monodisperse iron oxide nanoparticles prepared by a seeded-growth route. *Chemistry of Materials*, *23*(18), pp.4170–4180.
4. Van, H.N., Tam, P.D., Kien, N.D.T., Huy, P.T. and Pham, V.H., **2017**. Enhancing the luminescence of Eu3+/Eu2+ ion-doped hydroxyapatite by fluoridation and thermal annealing. *Luminescence*, *32*(5), pp.817–823.
5. Mahabole, M.P., Mene, R.U. and Khairnar, R.S., **2013**. Gas sensing and dielectric studies on cobalt doped hydroxyapatite thick films. *Advanced Materials Letters*, *4*(1), pp. 46–52.
6. Kumar, P.N., Mishra, S.K., Kiran, R.U. and Kannan, S., **2015**. Preferential occupancy of strontium in the hydroxyapatite lattice in biphasic mixtures formed from non-stoichiometric calcium apatites. *Dalton Transactions*, *44*(17), pp.8284–8292.
7. Kannan, S., Goetz-Neunhoeffer, F., Neubauer, J., Pina, S. and Ferreira, J.M.F., **2010**. Synthesis and structural characterization of strontium- and magnesium-co-substituted β-tricalcium phosphate. *Acta Biomaterialia*, *6*(2), pp.571–576.
8. Stojanović, Z., Veselinović, L., Marković, S., Ignjatović, N. and Uskoković, D., **2009**. Hydrothermal synthesis of nanosized pure and

cobalt-exchanged hydroxyapatite. *Materials and Manufacturing Processes*, *24*(10–11), pp.1096–1103.

9. Wu, H.C., Wang, T.W., Sun, J.S., Wang, W.H. and Lin, F.H., **2007**. A novel biomagnetic nanoparticle based on hydroxyapatite. *Nanotechnology*, *18*(16), p.165601.

10. Alshemary, A.Z., Akram, M., Goh, Y.F., Tariq, U., Butt, F.K., Abdolahi, A. and Hussain, R., **2015**. Synthesis, characterization, *in vitro* bioactivity and antimicrobial activity of magnesium and nickel doped silicate hydroxyapatite. *Ceramics International*, *41*(9), pp.11886–11898.

11. Águilaa, M.J.R., Avendañob, J.A.R. and Mendoza, M.E., **2017**. Structural analysis of metal-doped (Mn, Fe, Co, Ni, Cu, Zn) calcium hydroxyapatite synthetized by a sol–gel microwave-assisted method. *Ceramics International, 43*, pp.12706–12709.

12. Salehi, M.S.M., Nassaj, E.T. and Zori, M.H., **2018**. Effect of dopant (Co, Ni) concentration and hydroxyapatite compositing on photocatalytic activity of titania towards dye degradation. *Journal of Photochemistry and Photobiology A: Chemistry*, 356, pp.57–70.

13. Kamieniak, J., Kelly, P. J., Doyle, A.M. and Banks, C.E. **2018**. Influence of the metal/metal oxide redox cycle on the catalytic activity of methane oxidation over Pd and Ni doped hydroxyapatite. *Catalysis Communications*, 107, pp.82–86.

14. Baradaran, S., Moghaddam, E., Tabrizi, B.N., Basirun, W.J., Mehrali, M., Sookhakian, M., Hamdi, M. and Alias, Y., **2015**. Characterization of nickel-doped biphasic calcium phosphate/graphene nanoplatelet composites for biomedical application. *Materials Science and Engineering C, 49*, pp.656–668.

15. Poinern, G.J.E., Brundavanam, R.L.X.T., Le, X.T., Djordjevic, S., Prokic, M. and Fawcett, D., **2011**. Thermal and ultrasonic influence in the formation of nanometer scale hydroxyapatite bio-ceramic. *International Journal of Nanomedicine, 6*, p.2083.

16. Gopi, D., Ansari, M.T., Shinyjoy, E. and Kavitha, L., **2012**. Synthesis and spectroscopic characterization of magnetic hydroxyapatite nanocomposite using ultrasonic irradiation. *Spectrochimica Acta Part A: Molecular and Biomolecular Spectroscopy, 87*, pp.245–250.

17. Brundavanam, S., Poinern, G.E.J. and Fawcett, D., **2015**. Kinetic and adsorption behaviour of aqueous Fe^{2+}, Cu^{2+} and Zn^{2+} using a 30 nm hydroxyapatite based powder synthesized via a combined ultrasound and microwave based technique. *American Journal of Materials Science*, *5*(2), pp.31–40.

18. Robles-Águila, M.J., Reyes-Avendaño, J.A. and Mendoza, M.E., **2017**. Structural analysis of metal-doped (Mn, Fe, Co, Ni, Cu, Zn) calcium hydroxyapatite synthetized by a sol–gel microwave-assisted method. *Ceramics International*, *43*(15), pp.12705–12709.

19. Wakamura, M., Kandori, K. and Ishikawa, T., **1998**. Surface composition of calcium hydroxyapatite modified with metal ions. *Colloids and Surfaces A: Physicochemical and Engineering Aspects*, *142*(1), pp.107–116.

20. Baradaran, S., Nasiri-Tabrizi, B., Shirazi, F.S., Saber-Samandari, S., Shahtalebi, S. and Basirun, W.J., **2018**. Wet chemistry approach to the preparation of tantalum-doped hydroxyapatite: Dopant content effects. *Ceramics International*, *44*(3), pp.2768–2781.

21. Yuan, Q., Wu, J., Qin, C., Xu, A., Zhang, Z., Lin, Y., Chen, Z., Lin, S., Yuan, Z., Ren, X. and Zhang, P., **2017**. One-pot synthesis and characterization of Zn-doped hydroxyapatite nanocomposites. *Materials Chemistry and Physics, 199*, pp.122–130.

22. Boda, S.K., Basu, B. and Sahoo, B., **2015**. Structural and magnetic phase transformations of hydroxyapatite-magnetite composites under inert and ambient sintering atmospheres. *The Journal of Physical Chemistry C*, *119*(12), pp.6539–6555.

23. Tampieri, A., D'Alessandro, T., Sandri, M., Sprio, S., Landi, E., Bertinetti, L., Panseri, S., Pepponi, G., Goettlicher, J., Bañobre-López, M. and Rivas, J., **2012**. Intrinsic magnetism and hyperthermia in bioactive Fe-doped hydroxyapatite. *Acta Biomaterialia*, *8*(2), pp.843–851.

24. Yılmaz, B. and Evis, Z. **2014**. Raman spectroscopy investigation of nano hydroxyapatite doped with yttrium and fluoride ions. *Spectroscopy Letters, 47*, pp.24–29.

25. Lin, Y., Yang, Z. and Cheng, J. **2007**. Preparation, characterization and antibacterial property of cerium substituted hydroxyapatite nanoparticles. *Journal of Rare Earths*, *25*(4), pp.452–456.

26. Lee, D.K., Park, J.Y., Kim, M.R. and Jang, D.J., **2011**. Facile hydrothermal fabrication of hollow hexagonal hydroxyapatite prisms. *CrystEngComm*, *13*(17), pp.5455–5459.

27. Ciobanu, C.S., Iconaru, S.L., Le Coustumer, P., Constantin, L.V. and Predoi, D., **2012**. Antibacterial activity of silver-doped hydroxyapatite nanoparticles against gram-positive and gram-negative bacteria. *Nanoscale Research Letters*, *7*(1), p.324.

28. Tounsi, H., Djemal, S., Petitto, C. and Delahay, G., **2011**. Copper loaded hydroxyapatite catalyst for selective catalytic reduction of nitric oxide with ammonia. *Applied Catalysis B: Environmental, 107*(1–2), pp.158–163.

29. Rulis, P., Ouyang, L. and Ching, W.Y., **2004**. Electronic structure and bonding in calcium apatite crystals: Hydroxyapatite, fluorapatite, chlorapatite, and bromapatite. *Physical Review B*, *70*(15), p.155104.

Received: 11 January 2019. Accepted: 3 April 2019.